Time-resolved photoemission study of the electronic structure and dynamics of chemisorbed alkali atoms on Ru(0001)

Shengmin Zhang,[1] Cong Wang,[1] Xuefeng Cui,[2] Yanan Wang,[2] Adam Argondizzo,[1] Jin Zhao,[1,2,3,*] and Hrvoje Petek[1,†]

[1]*Department of Physics and Astronomy and Pittsburgh Quantum Institute, University of Pittsburgh, Pittsburgh, Pennsylvania 15260, USA*

[2]*Department of Physics and ICQD/Hefei National Laboratory for Physical Sciences at Microscale, University of Science and Technology of China, Hefei, Anhui, 230026, China*

[3]*Synergetic Innovation Center of Quantum Information & Quantum Physics, University of Science and Technology of China, Hefei, Anhui 230026, China*

(Received 25 October 2015; revised manuscript received 13 December 2015; published 5 January 2016)

We investigate the electronic structure and photoexcitation dynamics of alkali atoms (Rb and Cs) chemisorbed on transition-metal Ru(0001) single-crystal surface by angle- and time-resolved multiphoton photoemission. Three- and four-photon photoemission (3PP and 4PP) spectroscopic features due to the σ and π resonances arising from the ns and np states of free alkali atoms are observed from ~2 eV below the vacuum level in the zero-coverage limit. As the alkali coverage is increased to a maximum of 0.02 monolayers, the resonances are stabilized by formation of a surface dipole layer, but in contrast to alkali chemisorption on noble metals, both resonances form dispersive bands with nearly free-electron mass. Density functional theory calculations attribute the band formation to substrate-mediated interaction involving hybridization with the unoccupied d bands of the substrate. Time-resolved measurements quantify the phase and population relaxation times in the three-photon photoemission (3PP) process via the σ and π resonances. Differences between alkali-atom chemisorption on noble and transition metals are discussed.

DOI: 10.1103/PhysRevB.93.045401

I. INTRODUCTION

Alkali-atom chemisorption on metals has been a source of seminal ideas in surface science [1–12]. The dominant interaction leading to chemisorption of alkali atoms is between their valence ns electron and the free electrons of the metal substrate that is mediated by the Coulomb field. At a surface-atom distance of a few angstroms, the Coulomb image-charge interactions lift the alkali ns electron above the Fermi level; this causes the ns electron to transfer from alkali atom into the unoccupied levels of the substrate on the femtosecond time scale and, consequently, the atom to chemisorb in a predominantly ionic state [9,11,13]. The strong surface dipole formed by the ionic alkali atoms and their displaced electrons creates a surface potential, which causes a characteristic decrease of the surface work function [14]; this characteristic of alkali-atom-modified metal surfaces has found many applications in thermionic emission, catalysis, etc. [8,15].

The nature of the alkali-atom–metal surface bond, specifically, whether it should be described as ionic or covalent, however, has been a subject of a long-standing debate [7,16–18]. The lack of a distinct occupied electronic structure that could be diagnostic for the nature of the surface chemical bond has frustrated consensus [16]. Spectroscopic signatures of alkali-atom chemisorption were revealed, however, by methods that probe the unoccupied surface electronic structure such as the inelastic electron scattering [19], inverse photoemission [20,21], and two-photon photoemission (2PP) [22–24]. These techniques found a pronounced and sharp resonance approximately 2 eV below the vacuum level in the limit of zero alkali coverage, which has been assigned to the unoccupied ns state [11,23,24].

The spectroscopy and dynamics of the ns state (σ resonance) has been particularly interesting because of its exceptionally long lifetimes (~50 fs) for a strongly chemisorbed species [24–26]. On the (111) surfaces of noble metals, the restricted phase space as well as large polarizability stabilize the σ resonance with respect to decay by the elastic charge transfer from alkali atoms into the resonant bands of the substrate. The L projected band gaps on the Cu(111) and Ag(111) surfaces restrict the penetration and decay of the σ resonance into the resonant bulk bands that exist only for large values of parallel momentum $k_{||}$ [26–28].

The photoinduced charge transfer excitation of the σ resonance creates a neutral alkali atom at the nuclear distance of the chemisorbed ion [29]; this turns on strong Coulomb repulsion with the electrons in the Fermi sea that triggers the nuclear motion of alkali atom on the repulsive, antibonding potential surface [29–33]. In the case of Cs on Cu(111) and Ag(111) surfaces, the long lifetimes enabled surface femtochemistry of frustrated desorption to be observed and controlled on the sub-picosecond time scale [25,30–33].

In addition to the σ-resonance electronic structure theory predicted and 2PP experiments found another higher-lying state with predominantly np_x and np_y character (π resonance) about 0.3–0.7 eV above the σ resonance [34,35]. On Cu(111) and Ag(111) surfaces the atomic orbital character of this state was revealed by angle-resolved (AR) 2PP spectroscopy [34]: the two resonances appeared as nondispersive features with an intensity for $k_{||} = 0$ Å^{-1} being the maximum for the σ resonance and a local minimum (node) for the doubly degenerate π resonance. The angular photoelectron distributions were defined by m, the projection of the orbital angular momentum l onto the surface plane, where $m = 0$ for the σ resonance and $m = \pm 1$ for the π resonance. For coverages of <0.1 ML [we define one monolayer (ML) with respect to the substrate atom density], the nondispersive photoelectron angular distributions

*Corresponding author: zhaojin@ustc.edu.cn

†Corresponding author: petek@pitt.edu

indicated that the interadsorbate orbital overlap was too small to form a delocalized band [11,34,36].

Until now, most electronic structure studies of alkali-atom chemisorption have been performed on noble-metal surfaces [37]. Because the d bands of noble metals are 2–4 eV below the Fermi level, the electronic structure and dynamics of chemisorbed alkali atoms are primarily determined by interactions with the free-electron-like sp bands. The question of how the electronic structure of chemisorbed alkali atoms changes on the catalytically important transition-metal surfaces has hardly been addressed [38,39].

In this paper, we employ multidimensional multiphoton photoemission (mPP) spectroscopy to explore the unoccupied electronic structure of Rb and Cs at $\leqslant$0.02 ML coverage on a transition-metal surface Ru(0001). Because of its interesting properties in catalysis and surface femtochemistry, as well as substrate for graphene growth, the electronic structure and dynamics of alkali-atom-modified Ru(0001) surfaces are particularly interesting [40–46]. The electronic structure of Ru(0001) surface has been characterized by photoemission and inverse photoemission spectroscopy [47–49]. The bonding of alkali overlayers on Ru(0001) surface has been investigated by a variety of structural and spectroscopic techniques [10,44–46,50]. The chemisorption of Cs on Ru(0001) surface was found to stiffen the Cs-Ru bond as the coverage was increased, although the origin of this effect has not been fully explained [49]. To the best of our knowledge, however, the electronic structure of low-coverage alkali-atom-modified Ru(0001) surfaces has not been addressed by experiment or theory.

Using a broadly tunable femtosecond laser excitation source, we selectively detect the alkali-atom resonances in three- and four-photon photoemission (3PP and 4PP) processes (Fig. 1). Two-photon photoinduced electron transfer from the occupied d bands of Ru excites the σ and π resonances [29], which serve as the penultimate states in the 3PP process. Interferometric time-resolved (ITR) 3PP measurements provide information on the phase and energy relaxation times of the σ and π resonances. Surprisingly, AR-3PP spectra find strong dispersion of the σ and π bands at coverages where interatomic hybridization is unexpected based on the previous studies of alkalis on noble metals [11]. *Ab initio* calculations of the alkali-atom/Ru(0001) electronic structure attribute the dispersion to hybridization of the ns and $np_{x,y}$ orbitals of alkali atoms with the d bands of the substrate. Thus, our joint experiment-theory studies provide new information on the nature of alkali-atom–metal chemical bond.

II. EXPERIMENTAL METHODS

Multidimensional coherent multiphoton photoelectron spectroscopy experiments [52] are performed in a commercial ultrahigh vacuum chamber (UHV) with a base pressure of $<10^{-10}$ mbar. The Ru(0001) surface is prepared by repeated cycles of Ar ion sputtering and annealing at 1100 K in UHV. After preparation, the sample is cooled to $\sim$90 K by liquid nitrogen and then exposed to an effusive Cs or Rb atomic beam from commercial alkali-atom getter sources (SAES). The alkali-atom coverage is estimated from the observed work function decrease during the deposition using published calibration data [44,45,50].

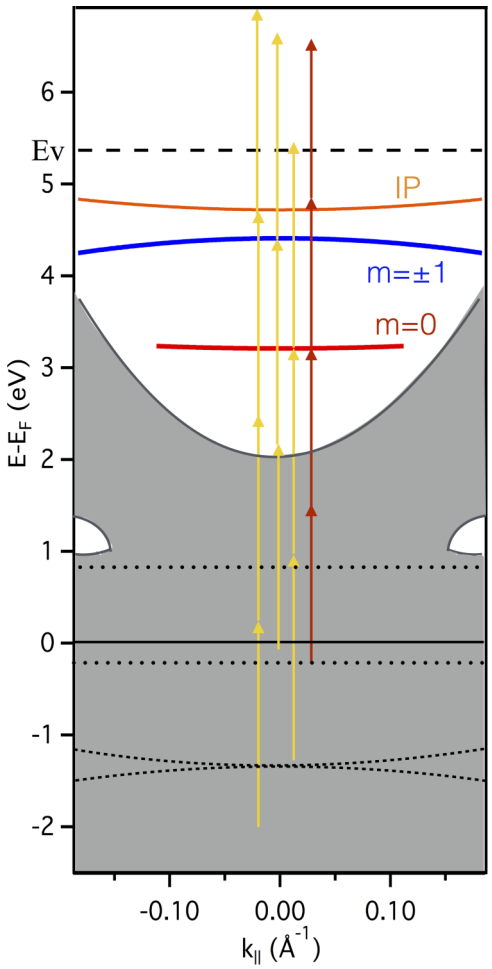

FIG. 1. The surface-projected band structure as a function of $k_{||}$ showing the 3PP and 4PP excitation processes through the alkali-induced resonance intermediate states. The yellow arrows show the possible transitions from d band of substrate Ru to $m = 0$ and ± 1 states with $\hbar\omega = 2.17$ eV light and the red arrows give the excitation processes with $\hbar\omega = 1.64$ eV light. The dashed or dotted horizontal lines indicate the d bands of Ru(0001) that have been observed or predicted by theory [47,48,51].

mPP spectra are excited with a noncollinear optical parametric amplifier (NOPA), which is pumped by a Clark MXR Impulse fiber laser oscillator-amplifier system. The NOPA operates at a 1.25-MHz repetition rate with $\sim$20 fs pulses and typical pulse energy of $<$60 nJ [52]. The fundamental output of the NOPA and its second harmonic can be tuned from 900 to 270 nm corresponding to 1.38–4.59 eV photon energy [53]. The pulse is compensated for positive dispersion in the optical path using multiple bounces from a pair of matched negative dispersion mirrors. The pulse duration is measured and optimized at the position of the sample by autocorrelation measurement using ITR-3PP signal from a polycrystalline Ta sample, which has a nearly instantaneous response (see Fig. S1 in the Supplemental Material [54]) [55].

AR-mPP spectra are recorded with a Specs Phoibos 150 electron energy analyzer, which is used in the $\pm 15^\circ$ angular acceptance mode. The images of photoelectron energy versus momentum [$E(k)$] are acquired in an electron counting mode using a delay-line detector. During the alkali-atom deposition,

mPP spectra (a combination of 3PP and 4PP) are recorded sequentially to characterize the σ and π resonances and the work function decrease. The deposition is terminated when the work function is reduced to the point where the signal from 2PP starts to overwhelm that from 3PP and 4PP. After the spectroscopic characterization, the photodynamics of alkali-atom excitation and relaxation are investigated by ITR-3PP. In this experimental mode, the delay between identical pump-probe pulses, which are produced in a self-made Mach-Zehnder interferometer (MZI), are scanned with a <50 as time-step resolution; at each step an $E(k)$ image is acquired [52,56,57]. Multiple pump-probe scans are acquired and accumulated for signal averaging to generate three-dimensional (3D) $E(k,t)$ movies of the coherent electron dynamics at alkali/Ru(0001) surfaces.

III. RESULTS AND DISCUSSION

Figure 1 shows the surface-projected band structure for Ru(0001) surface for a range of momenta around $k_{||} = 0$ Å^{-1} that we investigate. Based on electronic structure calculations, inverse photoemission, and 2PP spectroscopy, at the Γ point the Ru(0001) surface has a projected band gap that opens at ~2 eV and extends to at least 6 eV above the Fermi level E_F [47–49,58]. Near E_F, d bands have been reported at −0.1 and 1 eV also at the Γ point [48,59,60]. Band-structure calculations also predict a d band at 1.3 eV: these various features may have a role in mPP processes [48,51]. The work function of Ru(0001) is reported to be 5.4–5.5 eV [48,58]. Because the alkali-atom σ resonances are expected to occur in the low-coverage limit at ~2 eV below the vacuum level E_v, their coincidence with the band gap is favorable for studies of alkali-atom spectroscopy and dynamics. Figure 1 also shows some possible excitation pathways for 3PP and 4PP *via* the $n = 1$ image potential state (IP) on the bare Ru(0001) surface, as well as the σ and π resonances in the limit of low-alkali-atom coverage.

A. Analysis of mPP via alkali-atom resonances

Figures 2(a)–2(d) show two-dimensional $E(k)$ distribution images measured with 571 nm (2.17 eV) three- and

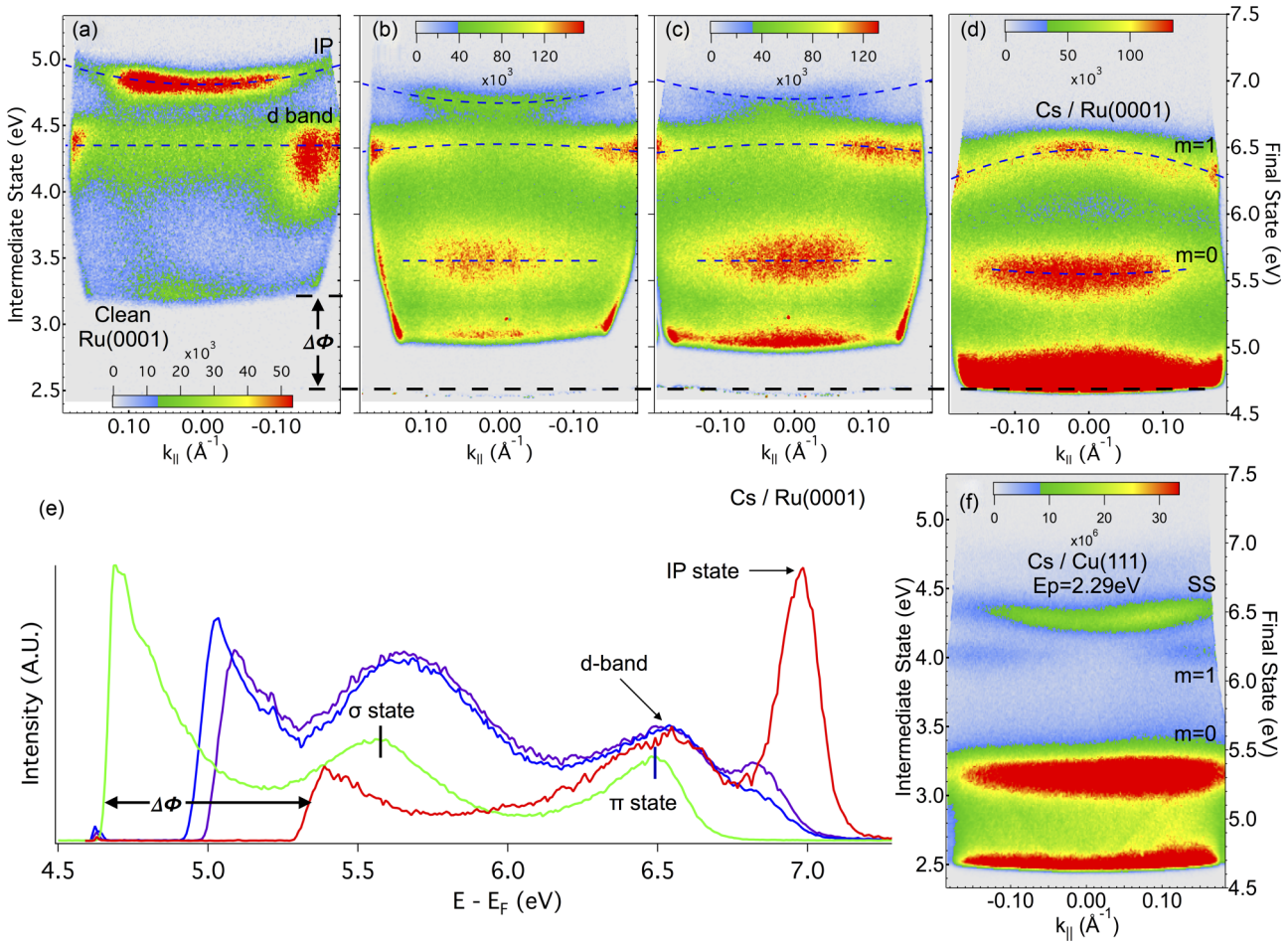

FIG. 2. (a)–(d) 3PP and 4PP spectra of the Ru(0001) surface excited $\hbar\omega = 2.17$ eV during the continuous deposition of Cs atoms starting from zero coverage. The spectra show the penultimate state energy (left axis) and the final photoelectron energy relative to E_F (right axis) versus the parallel momentum $k_{||}$. $\Delta\Phi$ gives the work function change before and after the deposition. The dashed straight or parabolic lines give the best fitting dispersions of specific bands. In (a) the fitting of the IP state gives $m^* = 1.1 \pm 0.02 m_e$ and in (d) the masses obtained for $m = 0$ and ± 1 are $m^* = 1.8 \pm 0.05 m_e$ and $-0.65 \pm 0.05 m_e$, respectively. (e) The line profiles of (a)–(d) that are taken at $k_{||} = 0$ Å^{-1}. (f) The 3PP spectrum with $\hbar\omega = 2.29$ eV excitation of Cs/Cu(111) surface is given to contrast with the Cs/Ru(0001) surface. SS indicates the occupied Shockley surface state of Cu(111).

four-photon excitation during deposition of Cs onto Ru(0001) surface. Cross sections through the $E(k)$ distributions for the normal emission ($k_{||} = 0$ Å^{-1}) are shown in Fig. 2(e) for more quantitative visualization of the data. The momentum resolved measurements are taken along the Γ-K direction.

Before alkali deposition, an mPP spectrum from the clean Ru(0001) surface is recorded [Fig. 2(a)]. The work function Φ of the clean Ru(0001) surface is found to be 5.37 eV. The mPP spectrum is dominated by two spectroscopic features: (i) the $n = 1$ image potential state (IP), which is the penultimate level in 4PP; and (ii) a d band [59], which is an initial state in 3PP -0.1 eV below E_F. When the Ru(0001) surface is clean and well ordered, the strongest feature in the mPP spectrum [Fig. 2(a)] is the IP state: its intensity is stronger than the occupied d band, even though the d band is excited by a lower-order process. The IP state binding energy with respect to the vacuum level is $\sim 0.58 \pm 0.04$ eV, which is slightly smaller than the literature value of $\sim 0.64 \pm 0.03$ eV [58], and its dispersion is consistent with the effective mass $m^* = 1.1 \pm 0.02 m_e$, where m_e is the free-electron mass.

Cs adsorption causes substantial changes in the mPP spectra [Figs. 2(b)–2(d)]; the work function progressively decreases as the coverage of Cs atoms increases [marked as $\Delta\Phi$ in Figs. 2(b)–2(d)]. The work function is reduced by formation of a surface dipole layer, which introduces an additional attractive potential [14,15,61]. Furthermore, adsorption of Cs also causes the IP state intensity to wane and the σ and π resonances to wax. By comparing the work function change with the literature calibration curves for Cs/Ru(0001) [44,45,50], we estimate the maximum coverage in our measurements to approach 0.02 ML. Because Rb^+ has approximately the same size as Cs^+, we expect it to have very similar calibration curve [45,50]. For comparison with noble metals, we also show a single 3PP $E(k)$ image for Cs/Cu(111) with <0.01 ML coverage that is obtained under similar conditions as for Cs on Ru(0001) substrate [Fig. 2(f)].

By contrast with the previous 2PP spectroscopic measurements of alkali atoms on noble metals, which were obtained with 3.1-eV excitation, the 3PP and 4PP schemes with visible light (1.54–2.17 eV) enable both the σ and π resonances to be observed within the same nonlinear order of excitation in the zero alkali-atom coverage limit. Moreover, higher-order mPP spectra appear to select coherent excitations of surface states over bulk hot electron processes [52].

Because we are detecting the alkali resonances via an mPP process, it is important to establish their position in the multiphoton absorption ladder. This is done by plotting the measured final-state energy of the resonance versus the photon energy and evaluating the resulting slope and intercept from a linear fit to the data. For reference, in Fig. 3 we first consider the $n = 1$ IP state on the clean Ru(0001) surface because being close to E_v it always takes one photon to detect in both the 3PP and 4PP schemes. In Fig. 3, we also plot the final-state energies of the σ and π resonances for the excitation with 1.54–2.27 eV photon energy pulses. In the 5–7 eV range of the final states, the resonances are detected in either 3PP or 4PP. In the case of 3PP ($\hbar\omega > 1.8$ eV), the excitation photon energy is sufficient to excite the σ and π resonances by a two-photon transition, followed by single-photon photoemission. Hence, the plots have a slope of ~ 1. In the case of excitation for $1.54 < \hbar\omega <$ 1.8 eV, the photoemission occurs by 4PP and their detection requires two-photon adsorption; hence, the slope in Fig. 3 is ~ 2. Based on this analysis, we can estimate that the σ and π resonances of Cs participate in the mPP processes as intermediate states at 3.22 and 4.35 eV for the 0.015-ML alkali coverage of the measurements in Fig. 3 (Table I).

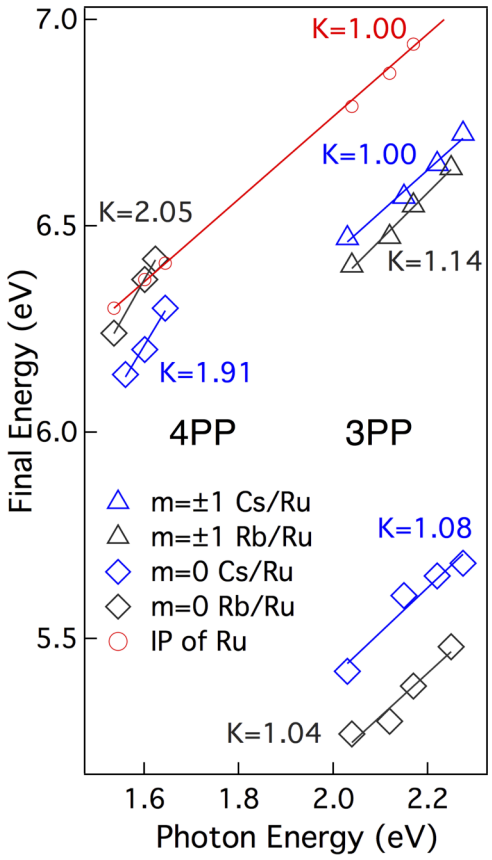

FIG. 3. The final states energy plotted as a function of photon energy with the linear fit. The slopes from fitting are marked in the figure correspondingly and the intercepts are summarized in Table I for $m = 0$ and ± 1 states. For the reference, the IP state of Ru(0001) is plotted.

To remove the effect of the surface dipole potential on the σ- and π-resonance energies, we must extrapolate the results to zero alkali coverage [11,36,62]. The change in the σ resonance with increasing coverage is evident in Figs. 2(b)–2(d). In the case of Cu(111) and Ag(111) surfaces,

TABLE I. The energies of σ and π resonances relative to E_F. m^* denotes the effective masses for the states from experiments and DFT calculations for the 6×6 Rb overlayer structure on Ru(0001). The binding energies are in the parentheses.

	E 0.015 ML[a]	E Zero limit[b]	$m^*_{\text{experimental}}$	$m^*_{\text{theoretical}}$
$m = 0$ Rb	3.12 eV	3.33 (−2.04) eV	$1.8 m_e$	$2.1 m_e$
$m = 0$ Cs	3.22 eV	3.59 (−1.78) eV	$1.8 m_e$	$1.5 m_e$
$m = \pm 1$ Rb	4.07 eV	4.13 (−1.24) eV	$-0.7 m_e$	$-0.7\ m_e$
$m = \pm 1$ Cs	4.36 eV	4.32 (−1.05) eV	$-0.65 m_e$	$-0.8 m_e$

[a]Intercepts from linear fitting in Fig. 3.
[b]Intercepts from linear fitting in Fig. 4.

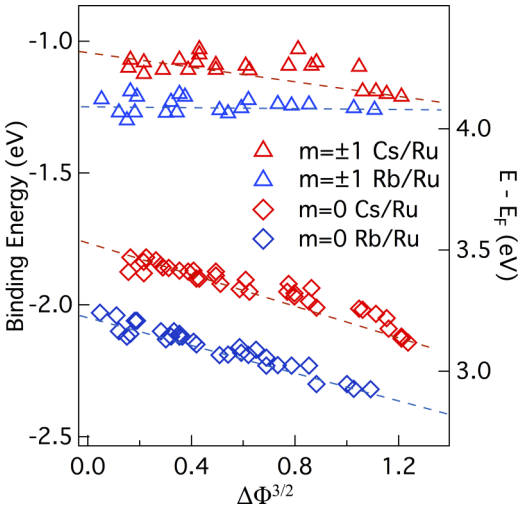

FIG. 4. The binding energies of $m = 0$ and ± 1 σ and π resonances relative to the vacuum level of the clean Ru(0001) surface (left axis) and E_F (right axis) for Rb and Cs on Ru(0001) surface, plotted versus work function change to the power of $\frac{3}{2}$ ($\Delta\Phi^{3/2}$). Dashed lines are linear fits to the data.

we have shown that the σ-resonance energy decreases linearly with respect to $\Delta\Phi^{3/2}$ [11,14,36,62,63]. In Fig. 4, we plot the σ- and π-resonance energies for Cs and Rb on Ru(0001) surface versus $\Delta\Phi^{3/2}$, and indeed find a linear trend. The dependence of the π-resonance energy on the alkali-atom coverage has not been measured previously: here we find it to decrease in energy but with a much weaker dependence on the coverage than the σ resonance. Because we expect that it should also respond to the dipole potential, this result suggests that another factor has a counteracting influence, as we will explain in the following.

From the linear fits to the data in Fig. 4 (dashed lines), we can extrapolate the σ- and π-resonance energies for Cs/Ru(0001) at the zero coverage limit to be 3.59 and 4.32 eV with respect to E_F, and -1.78 and -1.05 eV with respect to E_v. The corresponding analysis for Rb/Ru(0001) gives 3.33 and 4.13 eV with respect to E_F, and -2.04 and -1.24 eV with respect to E_v. Therefore, σ-π splittings for Cs and Rb are 0.73 and 0.80 eV on the Ru(0001) surface. For comparison, the zero coverage σ-π splitting for the Cu(111) surface in Fig. 2(f) is 0.87 ± 0.02 eV. The observed σ-π splittings for the Ru and Cu substrates in Figs. 2(f) and 4 are also comparable to the calculated zero-coverage splittings for noble-metal surfaces [34,35], although they are higher than 0.3–0.7 eV that we reported for higher alkali coverages on the Cu(111) and Ag(111) surfaces [34,36]. This discrepancy can be attributed to the overlap between the alkali resonances and the bands of the substrate, as well as lower experimental resolution of the previous experiments [34,36]; the mPP excitation and photoelectron imaging used in the present experiments provide more accurate splittings. For reference, the free atom ns to np excitation energies, i.e., the D lines of Cs and Rb in the absence of surface perturbation, are 1.39 and 1.56 eV. Thus, the larger splitting for Rb may be due to the larger s-p the atomic splitting. The resonance energies from the excitation wavelength and alkali-coverage-dependent measurements are reported in Table I.

B. Alkali resonance band formation

An unexpected feature of the σ- and π-resonance spectra in Figs. 2(b)–2(d) is that they form dispersive bands with effective masses that depend on the coverage. The dashed lines in Figs. 2(b)–2(d) indicate the band dispersions that are obtained by fitting parabolic curves to the peak maxima for different values of $k_{||}$. Similar dispersions are observed for the Rb/Ru(0001) surface. Fitting of σ and π bands in Fig. 2(d) gives effective masses of $m^* = 1.8 \pm 0.1 m_e$ and $-0.65 \pm 0.05 m_e$, respectively. At lower coverages, in Figs. 2(b) and 2(c), the σ band is still nondispersive, whereas the π-band effective mass is $-1.1 m_e$.

The observation of highly dispersive alkali-atom bands at low coverages on Ru(0001) surface is surprising because for noble metals the corresponding resonances are nondispersive even for coverages up to 0.1 ML [34]. Clearly, the alkali orbitals are able to interact at very low coverages on the Ru(0001) substrate. We observe a transition with coverage in the 2D spectra of Fig. 2 from where the angular intensity distributions reflect the localized orbital character of the $m = 0$ and ± 1 σ and π resonances, to a regime where angular band dispersion portend the delocalized orbital character. Specifically, in Figs. 2(b)–2(d) there is a progression where the node and antinode in the angular photoemission distributions for the π and σ resonances, respectively, disappear and are replaced by the band dispersions, which become stronger as the alkali coverage is increased. Thus, the orbital parentage of the two resonances is manifested in the spectra through a transitional regime where they change from the localized to a delocalized character. In the case of Cu(111) substrate, we observe the localized character under similar experimental conditions. Thus, the comparison between angular distributions for Ru(0001) and Cu(111) surfaces in Figs. 2(d) and 2(f) shows that the properties of the substrate significantly influence the σ- and π-resonance orbital interactions.

The observed effective masses are consistent with characteristics of bands formed by the in-plane σ bonding of s and p orbitals [64,65]. The $m = 0$ orbitals are bonding, have the band minimum at the Γ point, and their Bloch wave function has no nodes at $k_{||} = 0$ Å^{-1}. By contrast, the $m = \pm 1$ orbitals are antibonding, have the maximum at the Γ point, and their Bloch wave function has the maximum number of nodes. Thus, the band dispersions of alkali-induced states on Ru(0001) surface provide consistent evidence for the orbital origin of the σ and π resonances as the photoemission angular distributions for alkali-covered noble-metal surfaces, except for the former the electronic wave functions are delocalized, whereas for the latter they are localized. We will address the origin of these differences through electronic structure calculations.

In our analysis of the band dispersions, we assume that the interaction between alkali atoms at low coverage is purely repulsive due to dipole-dipole interaction, for which there is overwhelming evidence based on real and reciprocal space measurements [10,44,45,50,66,67]. Although Cs and Rb are bound by more than 3 eV at low coverage by ionic forces, the barriers for surface diffusion are in a few meV range

[50,68]. All measurements of the work function change versus alkali-atom coverage for Ru(0001) surface show a smooth change that is characteristic of increasing density of a hexactic liquid, rather than coverage-dependent order-disorder phase transitions that have been documented in a few cases for alkali chemisorption [10,69]. Moreover, we do not believe that there is preferential decoration of step edges at low coverage, based on STM measurements of Cs on noble-metal surfaces at comparable coverages [66,67].

Based on the above analysis, we note that there are two factors affecting the σ- and π- resonance energies at finite alkali-atom coverages. First, the increasing strength of the dipole potential as the alkali-atom coverage increases should lower the σ- and π-resonance energies by approximately the same amount. Second, the band formation at the Γ point stabilizes the bonding σ resonance and destabilizes the antibonding π resonance. The orbital interactions increase with the coverage because the magnitude of the effective mass decreases and the band curvature at the Γ point increases. Therefore, the two factors should enhance the stabilization of σ resonance and counteract the stabilization of the π resonance. We believe that the strong negative dispersion of the π resonance explains the different coverage-dependent tunings of the σ- and π-resonance energies in Fig. 4.

Another aspect of 3PP spectra in Figs. 2(b)–2(d) is the large width of the σ resonance for both the Cs and Rb/Ru(0001) surfaces. The origin of the width could be the coupling of the surface resonance to the resonant bulk bands for finite values of $k_{||}$, as can be expected from Fig. 1. For example, such broadening was found for Cs/Cu(100), where the σ resonance is similarly close to the bulk band edge [33,58,70]. An additional factor that may influence the σ-resonance width are possible resonances in optical transitions involving the d bands of the substrate. Specifically, an unoccupied d band with significant width has been reported at 0.9–1.0 eV above E_F in both the inverse photoemission and 2PP spectra of clean and graphene modified Ru(0001) surface [59,60]. It is likely that the σ resonance is excited by a one-photon transition from this intermediate d band, as suggested in Fig. 1, and therefore, the observed spectral width has contributions from the joint density of the coupled states in the 3PP process.

C. Theoretical analysis of the alkali-Ru bonding and band formation

The band formation of the σ and π resonances at coverages where through space interactions are expected to be too weak for electron delocalization suggests that the substrate could mediate the interactions. This points to a different character of alkali atom bonding to a transition-metal surface Ru(0001) than was found for noble metals [12,35,71,72].

To further understand the differences in alkali-atom interactions with Ru(0001) and Cu(111) surfaces, we performed first-principles electronic structure calculations for both Rb and Cs on Ru(0001) surface. The results of both alkali atoms are essentially the same and we will use the model of Rb on Ru(0001) to explain the details in the following text. DFT calculations are not expected to predict accurately the resonance energies of alkali atoms on metal surface because the image potential is not included [11,73]. Because the image potential is homogeneous within the 2D surface, however, we expect the errors in predicting band dispersions to be insignificant. Therefore, DFT calculations provide useful information on the comparative tendency of the σ and π resonances to form bands on the Ru(0001) and Cu(111) surfaces. The calculated effective masses for both Rb and Cs on Ru(0001) surface are in Table I and the band structure for Rb/Ru is in Fig. 5.

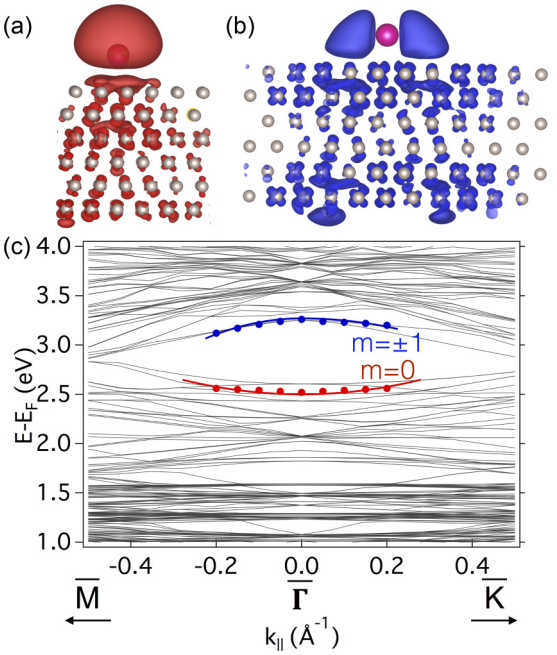

FIG. 5. (a), (b) The spatial orbital distributions of the $m = 0$ and ± 1 σ and π resonances of Rb atom on Ru(0001) surface. (c) The calculated electronic band structure of Rb on Ru(0001) using a 6×6 supercell. The red and blue dots and lines indicate the calculated σ- and π-resonance bands.

DFT calculations are carried out using plane-wave basis sets with cutoff energies of 250 eV for both Rb and Cs on Ru(0001) surface and 340 eV for Rb/Cu(111) using the generalized gradient approximation with PBE functional [74] as implemented in VASP [75–77]. The projector augmented wave method is used to describe the electron-ion interaction [78]. A six-layer slab model is used with a vacuum of 26 Å to avoid the interlayer interaction. Because the unit cell is as large as 16.2×16.2 Å^2, the Brillouin zone is sampled only at the Γ point.

We use a 6×6 supercell to simulate the surface, which contains 36 Ru atoms per layer: this corresponds to 0.03 ML Rb coverage. Rb atoms are in the hcp position, as dictated by previous low-energy electron diffraction studies [10]. Relative to the clean Ru(0001) surface, the calculated work function decrease is 1.0 eV, which is comparable to experiments. In Fig. 5(c), we show the surface projected band structure of Rb/Ru(0001). By comparing the projected density of states to the Rb covered Ru(0001) surface with the clean one, we identified the bands with contributions from the s and $p_{x,y}$ orbitals of Rb around the Γ point; these bands are marked with red and blue dots in Fig. 5(c). The σ and π resonances are located at 2.5 and 3.3 eV above E_F. As we discussed above, we

expect these energies to be only in qualitative agreement with experiment. The dispersion, however, is meaningful and in agreement with the experiment. As expected, the σ resonance has a positive dispersion and the π resonance a negative one. We obtain the theoretical effective masses from parabolic fits to the band dispersions. For the σ resonance, the effective mass is $2.1m_e$, whereas for the π resonance it depends on momentum. Specifically, it is $-0.7m_e$ along Γ-K and $-1.9m_e$ along Γ-M, whereas in Fig. 2 we measure along the Γ-K. For comparison, we have also calculated the band structures of Rb in a top position on Cu(111) using a 6×6 supercell, and find both the σ and π resonances to be nondispersive (see Fig. S2 in the Supplemental Material [54]). The same result is obtained when Rb is placed in a hollow site on Cu(111) surface.

The surface band structure results obtained by DFT calculations confirm that there is substrate-mediated interaction between low-density alkali atoms for the Ru(0001) but not for the Cu(111) surface. To understand this substrate effect, in Figs. 5(a) and 5(b) we plot the spatial distribution of orbitals that contribute to the σ and π resonances of Rb/Ru(0001) system. As in the case of alkali atoms on noble metals, the σ resonance has main contributions form the $5s$ and $5p_z$ orbitals, which hybridize in the presence of the surface. For the π resonance, the dominant contributions are from the Rb $5p_x$ and $5p_y$ orbitals, which hybridize with the Ru $3d_{xz}$ and $3d_{yz}$. The hybridization of Rb with the Cu(111) and Ru(0001) surfaces is different, however. For the adsorption of Rb on Ru(0001) one can see significant contribution from the d orbitals of Ru(0001) to both the σ and π resonances [Figs. 5(a) and 5(b)]. By contrast, for Cu(111) there is only small contribution from the s and p orbitals (Fig. S1b). For both surfaces, we expect that the resonant sp bands of the substrates interact weakly with the adsorbates due to presence of the band gaps. The difference between Ru(0001) and Cu(111) are the energies and bandwidths of the d bands. For Ru, the $4d$ bands extend from -6.0 eV to as high as 1.5 eV relative to E_F according to our DFT calculations. In the case of Cu, the $3d$ bands spread from -5.0 to -2.0 eV below the E_F; they are fully occupied and have a narrower bandwidth than for Ru(0001) [79]. Therefore, the empty $4d$ bands on Ru(0001) are much closer in energy to the alkali-induced resonances, and are more diffuse than the $3d$ bands of Cu(111). This enables more effectively hybridization of the σ and π resonances via the interactions with the d bands of the Ru(0001) substrate. This explains the strong substrate-mediated dispersion of the σ and π resonances, and points to a different character of alkali chemisorption on transition metals.

D. Ultrafast photoexcitation dynamics

Furthermore, we explored the photoexcitation dynamics for both the alkali-induced resonances of Cs and Rb by recording interferometric two-pulse correlation measurements (I2PC) [52]. Figure 6(a) shows an experimental 2D interferogram for $k_{||} = 0$ Å^{-1}, which is extracted from a 3D $E(k,t)$ movie for the Cs/Ru(0001) system under approximately the same conditions as in Fig. 2(d) using 2.14-eV excitation. Figures 7(a) and 7(b) show cross sections through the data in Fig. 6(a) at the energies of the σ and π resonances, which are indicated by the red and blue lines through Fig. 6(a). These I2PC scans reflect the electron dynamics associated with the coherent and incoherent 3PP excitation pathways involving the σ and π resonances.

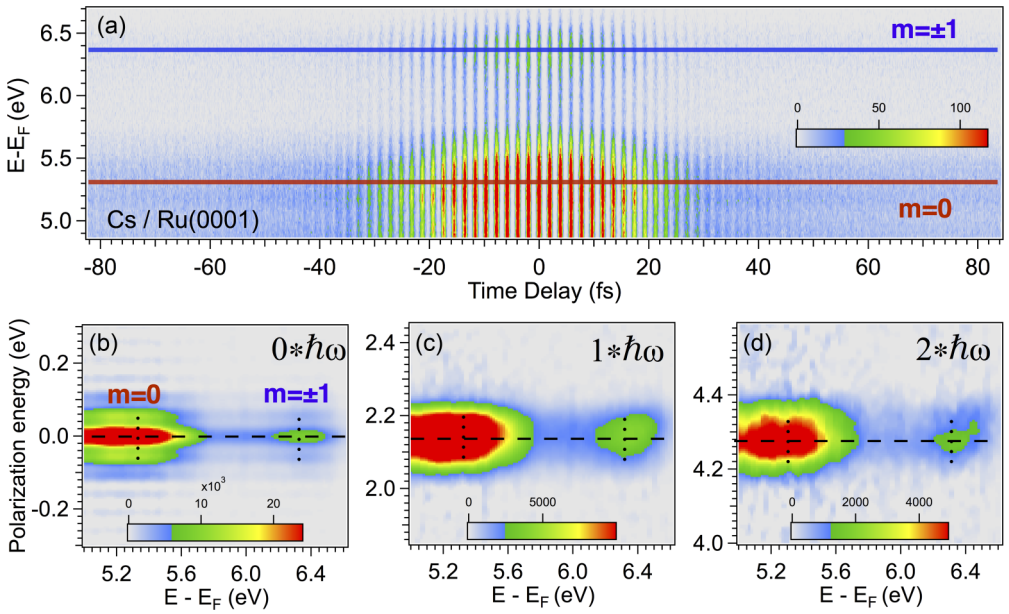

FIG. 6. (a) An interferogram representing a cut through a 3D movie $[E(k,t)]$ of mPP from Cs/Ru(0001) surface for $k_{||} = 0$ Å^{-1}. The measurement is performed with $\hbar\omega = 2.14$ eV for ~0.015 ML Cs/Ru(0001) at 90 K. The red and blue lines indicate the energies of $m = 0$ and ± 1 σ and π resonances where cuts through the interferogram give the I2PC scans in Fig. 7. (b)–(d) The 2D photoelectron spectra obtained by Fourier transforming interferometric scan in (a) showing individually components at zero frequency (b) and first (c) and second (d) harmonics of the laser frequency $\hbar\omega$. The horizontal dashed lines indicate the laser energy $\hbar\omega$ with different polarization orders. The vertical dotted lines indicate the final energy of σ and π resonances.

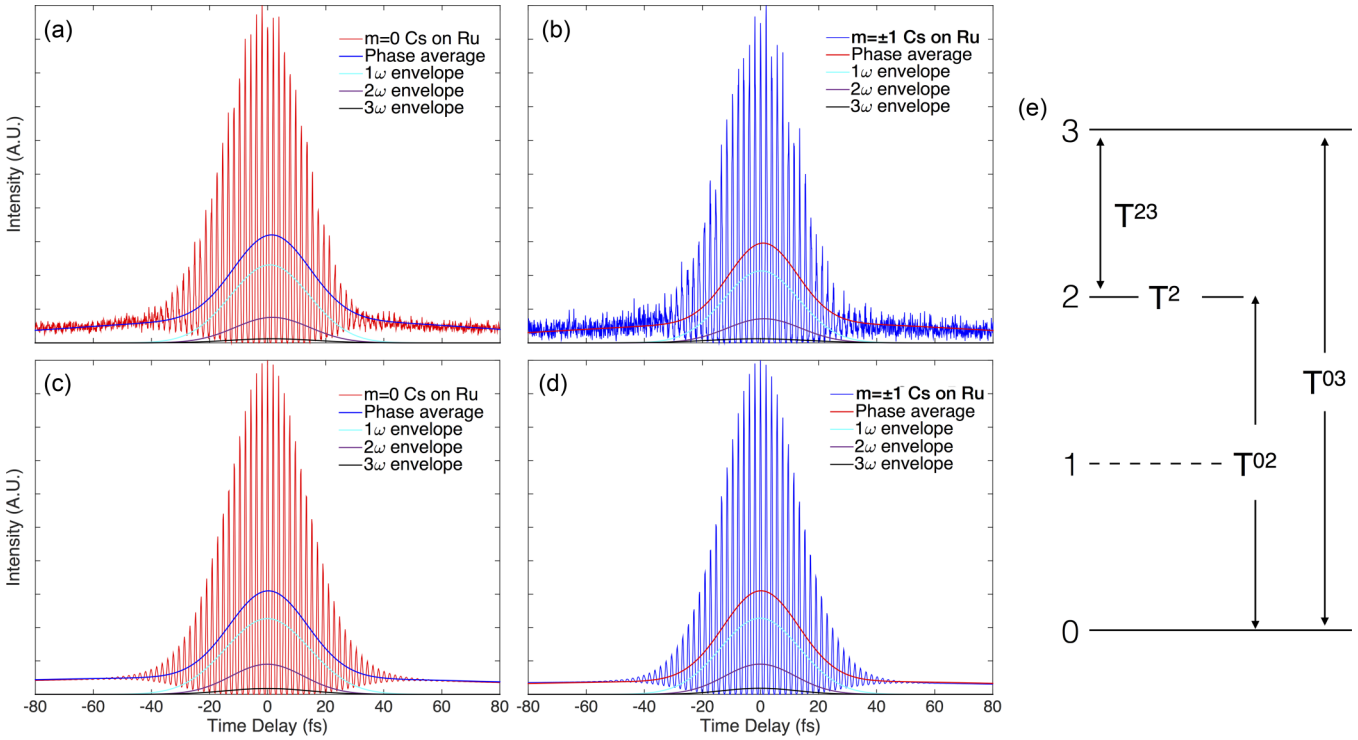

FIG. 7. (a), (b) I2PC scans for the σ and π resonances obtained from the interferogram in Fig. 6(a) for Cs/Ru(0001). The signal is decomposed into envelopes of components oscillating with different frequencies (see text in details), which are used to fit the polarization and population decay parameters. (c), (d) The simulated I2PC signals for these two resonances form a fit to an OBE model. (e) The diagram of four-level excitation.

A graphic way to evaluate the polarization and population dynamics associated with the 3PP process in Fig. 6(a) is by performing a Fourier transform (FT) of the data with respect to time. The result of this analysis gives the 2D FT images of the coherent linear and nonlinear polarization involved in the 3PP process versus the final-state energy, which are shown in Figs. 6(b)–6(d). The FT signal has components from the incoherent population dynamics ($0 * \hbar\omega_l$), the coherent polarization at the fundamental frequency ($1 * \hbar\omega_l$), and at its second harmonic frequency ($2 * \hbar\omega_l$), which are plotted versus the photoelectron energy. The $3 * \hbar\omega_l$ component, which also contributes to the 3PP process, is too weak to consider in the present analysis. The $0 * \hbar\omega_l$ component is sensitive to the incoherent population dynamics of electrons promoted to the intermediate states, whereas the $1 * \hbar\omega_l$ and $2 * \hbar\omega_l$ components reflect the linear and second-order nonlinear polarizations that contribute to the coherent pathways in the 3PP process.

The 2D plots give a correlation between populations and polarization frequencies excited in the sample and the final photoelectron state spectra where the mPP process terminates [52]. In a purely coherent process, the slope by which a 2D spectral feature tilts should reflect the order of the coherent process. For example, in a 3PP process from an initial state that is localized in energy, we expect a coherent three-photon absorption to have a slope of $\frac{1}{3}$ in Fig. 6(e) because three photons corresponding to polarization at a particular energy (abscissa) sum to generate the signal at the corresponding final-state energy (ordinate). In the case of inhomogeneous broadening, however, for example if the initial state is a d band, which disperses with perpendicular momentum, different polarization energies within the laser pulse can contribute to the same final-state energy. As a result, the 2D spectra do not tilt and a vertical cross section through a 2D spectrum at $1 * \hbar\omega_l$ just reflects the laser spectrum. The 2D spectra can also be influenced by dephasing in the intermediate states, which leads to loss of phase memory in the mPP process. In this case, the 2D spectra have tilted and horizontal contributions from the coherent and the dephased processes [52].

Examining the 2D spectra for the linear and second-order polarizations in Figs. 6(c) and 6(d), we find them to be essentially flat except for the π resonance at the highest final-state energies. Based on the projected band structure in Fig. 1, we can assert that the σ resonance is excited from d bands at <1 eV below E_F possibility via a resonance with an unoccupied d band at 0.9–1 eV above E_F. These bulk contributions probably contribute to the inhomogeneous broadening and hence explain in part the lack of tilting of the σ-resonance signal in the 2D spectra in Figs. 6(c) and 6(d). In the case of the π resonance, the slight tilting of the 2D spectra can be attributed to excitation from a narrow region about E_F. Because the phase space for electron-electron (e-e) scattering goes to zero at E_F and $T = 0$, and it grows rapidly with $(E - E_F)^2$ dependence away from E_F [55,58,80], the polarization associated with excitation form or to E_F is expected to dephase relatively slowly. Similar reduced dephasing rate for initial states near E_F is commonly observed in I2PC scans [81]. Therefore, we expect the two-photon coherence excited from the substrate bands at E_F to the π resonance to be somewhat protected

from the effects of inhomogeneous broadening and *e-e* scattering.

In Fig. 7, we analyze the alkali resonance photoexcitation dynamics with an optical Bloch equation (OBE) approach. We note that the OBE approach is only rigorous for an isolated system where local field effects are not important, and that it is difficult to treat inhomogeneous broadening that is inherent to a solid state or surface system [52,82]. Therefore, here we assume a minimal system for OBE simulation with the understanding that the extracted dephasing times are effective parameters, and should not be taken as a precise measurement of dephasing of the alkali atom σ and π resonances. The excited-state population lifetimes are more meaningful, except that the parameters could be associated with either the intermediate d band or alkali resonance states, which are excited by one or two photon processes. In this case, we assume that the bulk d-band lifetime is shorter than the alkali surface state lifetime; this assumption is grounded in extensive literature on the electron relaxation in metals and metal surfaces [25,57,60,83].

The OBE simulation is based on the data for Cs/Ru(0001) in Figs. 7(a) and 7(b), which corresponds to the I2PC cross sections from Fig. 6(a) at the σ- and π-resonance energies for $k_{||} = 0$ Å^{-1}. The I2PC results are similar for other photoemission angles. The corresponding simulated I2PC simulation results are given in Figs. 7(c) and 7(d). The energy level scheme and the key parameters for the simulation are given in Fig. 7(e). We use a four-level scheme, where "0" and "3" are the initial and the final states, "1" is virtual, and "2" is the alkali-atom resonance. Treating "1" as a virtual state is reasonable if the intermediate d band dephasing a population decay is much faster than for the alkali resonances. The main parameters in the simulation are T^2, the alkali resonance population decay time, and T^{23}, T^{02}, and T^{03}, the dephasing times of the linear, second-order, and third-order polarizations. The simulation is performed using a similar analysis method as in Ref. [57], where the I2PC signal is decomposed into the phase average, and the envelopes of the ω, 2ω, and 3ω oscillating. In order to simulate the experimental I2PC scans, the OBE calculation is performed until the calculated envelopes reproduce the experimental ones. In the simulation, the autocorrelation of the laser pulse is decomposed with the same method as described above, and the pulse duration is ~20 fs based on the analysis from the envelopes for the polycrystalline tantalum sample holder (Fig. S1 in Supplemental Material [54]). For the nonoscillating wings in the autocorrelation trace, we consider that the laser has a liner chirp. To obtain the information of the population and coherent decay of the alkali resonances more precisely, we include linear chirp term into the electric field of our laser pulse. Table II presents the best-fit parameters for Cs/Ru(0001) data in Fig. 7 and that obtained for Rb/Ru(0001) under similar coverage and laser excitation conditions.

The fitting results give approximately 40- and 20-fs lifetime for the Cs and Rb σ and π resonances on Ru(0001). With the caveat that these lifetimes could contain a contribution from the d bands of Ru(0001), we believe that these results are determined with an uncertainty of ~10 fs based on the sensitivity of the values on how the simulations are performed. The lifetimes of the σ resonances are similar, though faster, than those measured for the Cu(111) surface where a nonexponential decay due to the nuclear motion on the excited-state potential surface was consistent with a 50-fs lifetime [25,30]. We expect a shorter lifetime for alkali atoms on Ru(0001) surface because the large density of states of the occupied and unoccupied d bands can enhance decay channels via inelastic electron scattering with respect to the Cu(111) [84]. As far as the dephasing times are concerned, we cannot exclude that the parameters are not significantly affected by systematic errors, such as the incomplete characterization of the laser pulse. Further experiments, such as the temperature dependence of the dephasing rates, would be necessary to confirm their physical significance.

TABLE II. The polarization and population decay parameters from the OBE simulation in Fig. 7.

	T^2 (fs)	T^{23} (fs)	T^{02} (fs)	T^{03} (fs)
$m = 0$ Rb	40	11	10	16
$m = 0$ Cs	39	8	6	4
$m = \pm 1$ Rb	24	3	14	17
$m = \pm 1$ Cs	22	3	9	13

IV. CONCLUSIONS

Using 3D angle- and time-resolved 3PP spectroscopy and electronic structure theory, we described the electronic structure and lifetimes of Cs and Rb at <0.02 ML coverage on the transition-metal Ru(0001) surface. We found the σ and π resonances at comparable binding energies with respect to the vacuum level as the same resonances on the Cu(111) and Ag(111) noble-metal surfaces. This similarity suggests that the ionic interactions between the alkali ions and Ru(0001) surface dominate the alkali chemisorption as on noble metals [11]. The energy separation between the σ and π resonances is larger than previously reported in 2PP measurements for noble metals, and in better agreement with the theoretical predictions [34–36]. This difference between previous measurements can be attributed in part to a lower alkali coverage used in the present experiments, the more favorable detection of the alkali resonances with 3PP and 4PP excitation schemes, and to a higher photoelectron spectroscopic resolution. The larger σ-π splitting than previously reported is confirmed for Cs/Cu(111) surface resonances.

Although the σ- and π-resonance binding energies in the zero-coverage limit are consistent with the ionic bonding, we find strong differences in the interaction among alkali atoms that are mediated by the Ru(0001) surface and point to significant hybridization with the d bands of the substrate. The σ and π resonances exhibit strong dispersions at coverages as low as <0.02 ML, which reflect their $m = 0$ and ± 1 orbital character. DFT calculations confirm the tendency for band formation and attribute it to hybridization of alkali-atom orbitals with the d bands of the substrate. Such interactions are expected to be stronger for transition metals than for noble metals because of higher energy and larger bandwidths of the d bands.

With increasing alkali-atom coverage, the binding energy is linearly proportional with $\Delta\Phi^{3/2}$ due to the formation of the dipole potential. The tuning of the energies is different for the σ and π resonances most likely due to additional influence of the band formation, which shifts their energies in the opposite direction at the Γ point.

Finally, we measured ITR-3PP data for the Cs and Rb/Ru(0001) surfaces in order to characterize the photoexcitation dynamics and alkali resonance lifetimes. The observed lifetimes of 40 and 20 fs for the σ and π resonances of Cs and Rb are consistent with a stronger inelastic decay channel due to the presence of *d* band near the Fermi level as compared to noble metals. Overall, the character of the alkali-atom transition-metal interactions shows strong influence of the *d* bands on the alkali-atom band dispersions and resonance lifetimes.

ACKNOWLEDGMENTS

The authors acknowledge DOE-BES Division of Chemical Sciences, Geosciences, and Biosciences Grant No. DE-SC0002313, NSFC (Grants No. 11322434 and No. 21421063), National Key Basic Research Program (Grant No. 2011CB921404) for financial support. Some calculations were performed at the Environmental Molecular Sciences Laboratory at the PNNL, a user facility sponsored by the DOE Office of Biological and Environmental Research.

[1] I. Langmuir, Phys. Rev. **43**, 224 (1933).
[2] R. W. Gurney, Phys. Rev. **47**, 479 (1935).
[3] E. W. Plummer and R. D. Young, Phys. Rev. B **1**, 2088 (1970).
[4] J. W. Gadzuk, J. K. Hartman, and T. N. Rhodin, Phys. Rev. B **4**, 241 (1971).
[5] N. D. Lang and A. R. Williams, Phys. Rev. B **18**, 616 (1978).
[6] J. P. Muscat and D. M. Newns, Surf. Sci. **84**, 262 (1979).
[7] H. Ishida, Phys. Rev. B **38**, 8006 (1988).
[8] H. P. Bonzel, A. M. Bradshaw, and G. Ertl, *Poisoning and Promotion in Catalysis based on Surface Science Concepts and Experiments* (Elsevier, Amsterdam, 1989).
[9] P. Nordlander and J. C. Tully, Phys. Rev. B **42**, 5564 (1990).
[10] R. D. Diehl and R. McGrath, J. Phys.: Condens. Matter **9**, 951 (1997).
[11] J. Zhao, N. Pontius, A. Winkelmann, V. Sametoglu, A. Kubo, A. G. Borisov, D. Sánchez-Portal, V. M. Silkin, E. V. Chulkov, P. M. Echenique, and H. Petek, Phys. Rev. B **78**, 085419 (2008).
[12] M. I. Trioni, S. Achilli, and E. V. Chulkov, Prog. Surf. Sci. **88**, 160 (2013).
[13] H. Winter, Phys. Rep. **367**, 387 (2002).
[14] J. Topping, J. Proc. R. Soc. London A **114**, 67 (1927).
[15] S. Yamamoto, Rep. Prog. Phys. **69**, 181 (2006).
[16] B. Woratschek, W. Sesselmann, J. Küppers, G. Ertl, and H. Haberland, Phys. Rev. Lett. **55**, 1231 (1985).
[17] G. K. Wertheim, D. M. Riffe, and P. H. Citrin, Phys. Rev. B **49**, 4834 (1994).
[18] C. Stampfl, J. Neugebauer, and M. Scheffler, Surf. Sci. **307-309, Part A**, 8 (1994).
[19] D. Heskett, K. H. Frank, E. E. Koch, and H. J. Freund, Phys. Rev. B **36**, 1276 (1987).
[20] R. Dudde, K. H. Frank, and B. Reihl, Phys. Rev. B **41**, 4897 (1990).
[21] D. A. Arena, F. G. Curti, and R. A. Bartynski, Phys. Rev. B **56**, 15404 (1997).
[22] H. B. Nielsen and W. Thowladda, Surf. Sci. **284**, L426 (1993).
[23] N. Fischer, S. Schuppler, T. Fauster, and W. Steinmann, Surf. Sci. **314**, 89 (1994).
[24] M. Bauer, S. Pawlik, and M. Aeschlimann, Phys. Rev. B **55**, 10040 (1997).
[25] S. Ogawa, H. Nagano, and H. Petek, Phys. Rev. Lett. **82**, 1931 (1999).
[26] J. P. Gauyacq, A. G. Borisov, G. Raseev, and A. K. Kazansky, Faraday Discuss. **117**, 15 (2000).
[27] A. G. Borisov, J. P. Gauyacq, A. K. Kazansky, E. V. Chulkov, V. M. Silkin, and P. M. Echenique, Phys. Rev. Lett. **86**, 488 (2001).
[28] A. G. Borisov, A. K. Kazansky, and J. P. Gauyacq, Phys. Rev. B **65**, 205414 (2002).
[29] H. Petek, J. Chem. Phys. **137**, 091704 (2012).
[30] H. Petek, M. J. Weida, H. Nagano, and S. Ogawa, Science **288**, 1402 (2000).
[31] H. Petek, H. Nagano, M. J. Weida, and S. Ogawa, J. Phys. Chem. A **104**, 10234 (2000).
[32] H. Petek, H. Nagano, M. J. Weida, and S. Ogawa, J. Phys. Chem. B **105**, 6767 (2001).
[33] H. Petek and S. Ogawa, Annu. Rev. Phys. Chem. **53**, 507 (2002).
[34] A. G. Borisov, V. Sametoglu, A. Winkelmann, A. Kubo, N. Pontius, J. Zhao, V. M. Silkin, J. P. Gauyacq, E. V. Chulkov, P. M. Echenique, and H. Petek, Phys. Rev. Lett. **101**, 266801 (2008).
[35] S. Achilli, M. I. Trioni, E. V. Chulkov, P. M. Echenique, V. Sametoglu, N. Pontius, A. Winkelmann, A. Kubo, J. Zhao, and H. Petek, Phys. Rev. B **80**, 245419 (2009).
[36] L. M. Wang, V. Sametoglu, A. Winkelmann, J. Zhao, and H. Petek, J. Phys. Chem. A **115**, 9479 (2011).
[37] J. P. Gauyacq, A. G. Borisov, and M. Bauer, Prog. Surf. Sci. **82**, 244 (2007).
[38] S. Ogawa, H. Nagano, and H. Petek, Phys. Rev. Lett. **88**, 116801 (2002).
[39] R. D. Muiño, D. Sánchez-Portal, V. M. Silkin, E. V. Chulkov, and P. M. Echenique, Proc. Natl. Acad. Sci. USA **108**, 971 (2011).
[40] G. H. Rocker, C. L. Cobb, C. Huang, H. Tochihara, H. Metiu, and R. M. Martin, Surf. Sci. Lett. **222**, A546 (1989).
[41] M. Bonn, S. Funk, C. Hess, D. N. Denzler, C. Stampfl, M. Scheffler, M. Wolf, and G. Ertl, Science **285**, 1042 (1999).
[42] H. Over, H. Bludau, R. Kose, and G. Ertl, Surf. Sci. **331-333, Part A**, 62 (1995).
[43] Y. Pan, H. Zhang, D. Shi, J. Sun, S. Du, F. Liu, and H. Gao, Adv. Mater. **21**, 2777 (2009).
[44] G. Pirug, C. Ritke, and H. P. Bonzel, Surf. Sci. **257**, 50 (1991).
[45] J. Hrbek, Surf. Sci. **164**, 139 (1985).
[46] P. He and K. Jacobi, Phys. Rev. B **53**, 3658 (1996).

[47] T. Pelzer, G. Ceballos, F. Zbikowski, B. Willerding, K. Wandelt, U. Thomann, C. Reuß, T. Fauster, and J. Braun, J. Phys.: Condens. Matter **12**, 2193 (2000).
[48] W. K. Siu and R. A. Bartynski, Phys. Rev. B **75**, 235427 (2007).
[49] N. Nguyen, M. Mulazzi, and F. Reinert, J. Electron Spectrosc. Relat. Phenom. **191**, 27 (2013).
[50] G. Rangelov and L. Surnev, Surf. Sci. **185**, 457 (1987).
[51] N. A. W. Holzwarth and J. R. Chelikowsky, Solid State Commun. **53**, 171 (1985).
[52] X. Cui, C. Wang, A. Argondizzo, S. Garrett-Roe, B. Gumhalter, and H. Petek, Nat. Phys. **10**, 505 (2014).
[53] A. Argondizzo, X. Cui, C. Wang, H. Sun, H. Shang, J. Zhao, and H. Petek, Phys. Rev. B **91**, 155429 (2015).
[54] See Supplemental Material at http://link.aps.org/supplemental/10.1103/PhysRevB.93.045401 for the pulse autocorrelation measurement and electronic structure calculations on Rb/Cu(111) surface.
[55] M. Bauer, A. Marienfeld, and M. Aeschlimann, Prog. Surf. Sci. **90**, 319 (2015).
[56] S. Ogawa, H. Nagano, H. Petek, and A. P. Heberle, Phys. Rev. Lett. **78**, 1339 (1997).
[57] H. Petek and S. Ogawa, Prog. Surf. Sci. **56**, 239 (1997).
[58] W. Berthold, U. Höfer, P. Feulner, and D. Menzel, Chem. Phys. **251**, 123 (2000).
[59] N. Armbrust, J. Güdde, P. Jakob, and U. Höfer, Phys. Rev. Lett. **108**, 056801 (2012).
[60] M. Lisowski, P. A. Loukakos, U. Bovensiepen, J. Stähler, C. Gahl, and M. Wolf, Appl. Phys. A **78**, 165 (2004).
[61] R. W. Verhoef and M. Asscher, Surf. Sci. **391**, 11 (1997).
[62] A. G. Borisov, A. K. Kazansky, and J. P. Gauyacq, Surf. Sci. **430**, 165 (1999).
[63] T. Aruga and Y. Murata, Prog. Surf. Sci. **31**, 61 (1989).
[64] R. Hoffmann, Rev. Mod. Phys. **60**, 601 (1988).
[65] J. Zhao, M. Feng, J. Yang, and H. Petek, ACS Nano **3**, 853 (2009).
[66] M. Ziegler, J. Kröger, R. Berndt, A. Filinov, and M. Bonitz, Phys. Rev. B **78**, 245427 (2008).
[67] T. von Hofe, J. Kröger, and R. Berndt, Phys. Rev. B **73**, 245434 (2006).
[68] A. P. Graham, Surf. Sci. Rep. **49**, 115 (2003).
[69] W. C. Fan and A. Ignatiev, J. Vac. Sci. Technol. A **6**, 735 (1988).
[70] M. Bauer, S. Pawlik, and M. Aeschlimann, Phys. Rev. B **60**, 5016 (1999).
[71] S. Achilli, M. I. Trioni, and G. P. Brivio, Phys. Rev. B **81**, 165444 (2010).
[72] S. Achilli, M. I. Trioni, and E. V. Chulkov, Phys. Rev. B **85**, 045408 (2012).
[73] J. Zhao, M. Feng, D. B. Dougherty, H. Sun, and H. Petek, ACS Nano **8**, 10988 (2014).
[74] J. P. Perdew, K. Burke, and M. Ernzerhof, Phys. Rev. Lett. **77**, 3865 (1996).
[75] G. Kresse and J. Hafner, Phys. Rev. B **47**, 558 (1993).
[76] G. Kresse and J. Hafner, Phys. Rev. B **48**, 13115 (1993).
[77] G. Kresse and J. Hafner, Phys. Rev. B **49**, 14251 (1994).
[78] G. Kresse and D. Joubert, Phys. Rev. B **59**, 1758 (1999).
[79] A. Winkelmann, C. Tusche, A. A. Ünal, M. Ellguth, J. Henk, and J. Kirschner, New J. Phys. **14**, 043009 (2012).
[80] S. Ogawa, H. Nagano, and H. Petek, Phys. Rev. B **55**, 10869 (1997).
[81] H. Petek, H. Nagano, M. J. Weida, and S. Ogawa, Chem. Phys. **251**, 71 (2000).
[82] M. J. Weida, S. Ogawa, H. Nagano, and H. Petek, J. Opt. Soc. Am. B **17**, 1443 (2000).
[83] P. M. Echenique, J. M. Pitarke, E. V. Chulkov, and A. Rubio, Chem. Phys. **251**, 1 (2000).
[84] A. G. Borisov, J. P. Gauyacq, E. V. Chulkov, V. M. Silkin, and P. M. Echenique, Phys. Rev. B **65**, 235434 (2002).